



# Study of dynamics of the process $e^+e^- \rightarrow \pi^+\pi^-\pi^0$ in the energy range 1.15–2.00 GeV

SND Collaboration

M. N. Achasov<sup>1,2</sup>, A. Yu. Barnyakov<sup>1,2</sup>, A. A. Baykov<sup>1,2</sup>, K. I. Beloborodov<sup>1,2</sup>, A. V. Berdyugin<sup>1,2</sup>, D. E. Berkaev<sup>1,2</sup>, A. G. Bogdanchikov<sup>1</sup>, A. A. Botov<sup>1</sup>, T. V. Dimova<sup>1,2,a</sup>, V. P. Druzhinin<sup>1,2</sup>, V. B. Golubev<sup>1</sup>, A. N. Kirpotin<sup>1</sup>, L. V. Kardapoltsev<sup>1,2</sup>, A. S. Kasaev<sup>1</sup>, A. G. Kharlamov<sup>1,2</sup>, I. A. Koop<sup>1,2</sup>, A. A. Korol<sup>1,2</sup>, D. P. Kovrizhin<sup>1</sup>, A. S. Kupich<sup>1</sup>, K. A. Martin<sup>1</sup>, N. A. Melnikova<sup>1</sup>, N. Yu. Muchnoy<sup>1,2</sup>, A. E. Obrazovsky<sup>1</sup>, E. V. Pakhtusova<sup>1</sup>, K. V. Pugachev<sup>1,2</sup>, D. V. Rabusov<sup>1</sup>, Yu. A. Rogovsky<sup>1,2</sup>, Y. S. Savchenko<sup>1,2</sup>, A. I. Senchenko<sup>1,2</sup>, S. I. Serednyakov<sup>1,2</sup>, D. N. Shatilov<sup>1</sup>, Yu. M. Shatunov<sup>1,2</sup>, D. A. Shtol<sup>1</sup>, D. B. Shwartz<sup>1,2</sup>, Z. K. Silagadze<sup>1,2</sup>, I. K. Surin<sup>1</sup>, M. V. Timoshenko<sup>1</sup>, Yu. V. Usov<sup>1</sup>, V. N. Zhabin<sup>1</sup>, V. V. Zhulanov<sup>1,2</sup>

<sup>1</sup> Budker Institute of Nuclear Physics, SB RAS, Novosibirsk 630090, Russia

<sup>2</sup> Novosibirsk State University, Novosibirsk 630090, Russia

Received: 30 July 2020 / Accepted: 6 October 2020 / Published online: 27 October 2020  
© The Author(s) 2020

**Abstract** The dynamics of the process  $e^+e^- \rightarrow \pi^+\pi^-\pi^0$  is studied in the energy region from 1.15 to 2.00 GeV using data accumulated with the SND detector at the VEPP-2000  $e^+e^-$  collider. The Dalitz plot distribution and  $\pi^+\pi^-$  mass spectrum are analyzed in a model including the intermediate states  $\rho(770)\pi$ ,  $\rho(1450)\pi$ , and  $\omega\pi^0$ . As a result, the energy dependences of the  $\rho(770)\pi$  and  $\rho(1450)\pi$  cross sections and the relative phases between the  $\rho(770)\pi$  amplitude and the  $\rho(1450)\pi$  and  $\omega\pi^0$  amplitudes are obtained. The  $\rho(1450)\pi$  cross section has a peak in the energy region of the  $\omega(1650)$  resonance (1.55–1.75 GeV). In this energy range the contributions of the  $\rho(770)\pi$  and  $\rho(1450)\pi$  states are of the same order of magnitude. No resonance structure near 1.65 GeV is observed in the  $\rho(770)\pi$  cross section. We conclude that the intermediate state  $\rho(1450)\pi$  gives a significant contribution to the decay of  $\omega(1650) \rightarrow \pi^+\pi^-\pi^0$ , whereas the  $\rho(770)\pi$  mechanism dominates in the decay  $\omega(1420) \rightarrow \pi^+\pi^-\pi^0$ .

## 1 Introduction

The process  $e^+e^- \rightarrow \pi^+\pi^-\pi^0$  was studied in many experiments. It was first observed in 1969 at the ACO  $e^+e^-$  collider [1] when scanning the energy region near the  $\omega(782)$  resonance. Currently the  $e^+e^- \rightarrow \pi^+\pi^-\pi^0$  cross section is

measured in detail in the center-of-mass (c.m.) energy ( $\sqrt{s}$ ) range from 0.6 GeV to 3 GeV. The most accurate data were obtained in the SND [2–5], CMD-2 [6,7], and BABAR [8] experiments. At higher energies, there are the measurements of the  $J/\psi \rightarrow \pi^+\pi^-\pi^0$  and  $\psi(2S) \rightarrow \pi^+\pi^-\pi^0$  decays [9], and the cross section at  $\sqrt{s} = 3.67$  and 3.77 GeV in the CLEO [10] experiment.

It is usually assumed that the transition through the  $\rho(770)\pi$  intermediate state dominates in the process  $e^+e^- \rightarrow \pi^+\pi^-\pi^0$ . Quantitative verification of this assumption was made only in resonances. In Ref. [11], the Dalitz plot distribution for the  $\omega \rightarrow 3\pi$  decay was analyzed. It was shown that the distribution is consistent with that for the  $\rho(770)\pi$  mechanism. In Ref. [12], the fraction of the  $\phi \rightarrow 3\pi$  decays proceeding through the  $\rho(770)\pi$  intermediate state was determined to be  $f_{\rho\pi} = 94\%$ . The fraction of the so-called “direct mechanism”, which can be interpreted also as the transition through the  $\rho(1450)\pi$  intermediate state, was found to be about 1%. The rest is the interference between these two amplitudes.

In the decay of  $J/\psi \rightarrow \pi^+\pi^-\pi^0$  [13], the contribution of the  $\rho(1450)\pi$  mechanism increases up to 11%, and  $f_{\rho\pi} \approx 114\%$ . The interference between the two amplitudes is destructive in this decay. The decay  $\psi(2S) \rightarrow \pi^+\pi^-\pi^0$  has an unusually low branching fraction,  $(2.01 \pm 0.17) \times 10^{-4}$  [9], which is an order of magnitude less than the estimate made from the  $J/\psi$  decay:  $B(\psi(2S) \rightarrow \pi^+\pi^-\pi^0) \approx B(J/\psi \rightarrow \pi^+\pi^-\pi^0)B(\psi(2S) \rightarrow e^+e^-)/B(J/\psi \rightarrow e^+e^-) = 2.8 \times 10^{-3}$ . Also unusual is the Dalitz plot dis-

<sup>a</sup>e-mail: baiert@inp.nsk.su (corresponding author)

tribution for this decay [14]. Most events are located in the center of the distribution, and the two-pion mass spectrum has a wide maximum near 2.2 GeV. The fraction of events containing  $\rho(770)$  is a few percent.

Therefore, it seems interesting to study the dynamics of the process  $e^+e^- \rightarrow \pi^+\pi^-\pi^0$  in the region  $\sqrt{s} = 1.1\text{--}2.0$  GeV, where there are two excited resonances of the  $\omega$  family:  $\omega(1420)$  and  $\omega(1650)$ . Two-pion invariant mass spectra for this energy region are given in Refs. [3, 8]. In the  $\pi^+\pi^-$  mass spectrum a narrow peak is seen near the  $\omega(782)$  mass, which is explained by the contribution of the process  $e^+e^- \rightarrow \omega\pi^0$  with the  $\omega$  decaying to  $\pi^+\pi^-$ . This phenomenon was predicted theoretically in Ref. [15]. In the energy range 1.1–1.4 GeV, two-pion mass spectra are well described by the sum of the  $\rho(770)\pi$  and  $\omega\pi^0$  intermediate states [3, 8]. However, in the range  $\sqrt{s} = 1.4\text{--}2.0$  GeV a significant deviation from this model is observed in the  $\pi^\pm\pi^0$  mass spectrum, which reveals in a shift of the  $\rho$ -meson peak position and a bump at mass about 1 GeV. In Ref. [8], the contribution of the  $\omega(1650) \rightarrow \rho(1450)\pi$  decay, which interferes with the  $\rho(770)\pi$  amplitude, is suggested as a possible explanation for this deviation.

The main goal of this work is to study the dynamics of the process  $e^+e^- \rightarrow \pi^+\pi^-\pi^0$  in the energy range from 1.15 GeV to 2.00 GeV using data accumulated in the SND experiment at the VEPP-2000  $e^+e^-$  collider [16].

## 2 Detector and experiment

The spherical neutral detector (SND) is an universal non-magnetic detector collecting data at the VEPP-2000  $e^+e^-$  collider. A detailed description of detector subsystems can be found in Refs. [17–20]. The main part of the detector is the three-layer spherical electromagnetic calorimeter based on NaI (Tl) crystals. The calorimeter covers 95% of the solid angle. Its energy resolution for photons is  $\sigma_E/E = 4.2\%/ \sqrt[4]{E(\text{GeV})}$ , and the angular resolution (r.m.s) is about  $1.5^\circ$ . Parameters of charged particles are measured using a nine-layer drift chamber and a single-layer proportional chamber with cathode strip readout located in a common gas volume. The solid angle of the tracking system is 94% of  $4\pi$ . Its angular resolution (r.m.s) is  $0.45^\circ$  and  $0.8^\circ$  for the azimuthal and polar angles, respectively. The muon system is located outside the calorimeter and consists of proportional tubes and scintillation counters.

The analysis is based on data recorded in the SND experiment in 2011 and 2012. Several scans of the energy region from 1.05 to 2.00 GeV with a total integrated luminosity of  $34 \text{ pb}^{-1}$  were performed with a step of 20–25 MeV. The 2011 data set was used previously [5] to measure the  $e^+e^- \rightarrow \pi^+\pi^-\pi^0$  cross section.

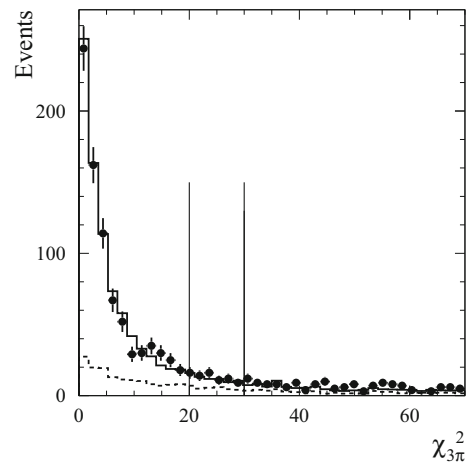


**Fig. 1** The  $\chi^2_{3\pi}$  distribution for data events with  $\sqrt{s} = 1.44$  GeV (points with error bars). The solid curve is a sum of simulated distributions for signal and background events. The dashed curve shows the background contribution. The simulated distributions are normalized to the numbers of signal and background events determined from the fit to the two-photon invariant mass distribution. The lines indicate the cuts used for cross section measurement ( $\chi^2_{3\pi} < 30$ ) and for dynamics study ( $\chi^2_{3\pi} < 20$ )

The luminosity in this analysis is measured using the process of elastic scattering  $e^+e^- \rightarrow e^+e^-$  with an accuracy better than 2% [5].

## 3 Event selection and measurement of the $e^+e^- \rightarrow \pi^+\pi^-\pi^0$ cross section

The selection of  $e^+e^- \rightarrow \pi^+\pi^-\pi^0$  candidate events is described in detail in Ref. [5]. The following criteria are applied. The candidate event contains two charged particles originating from the beam interaction region and two photons with energy higher than 30 MeV. The polar angles of the charged particles must be in the range from  $30^\circ$  to  $150^\circ$ . Background from the two-body processes  $e^+e^- \rightarrow e^+e^-$ ,  $\mu^+\mu^-$ ,  $\pi^+\pi^-$ , and  $K^+K^-$  is rejected by the condition  $|180^\circ - |\varphi_1 - \varphi_2|| > 10^\circ$ , where  $\varphi_i$  are the charged-particle azimuthal angles. To suppress beam-generated background and background from QED processes, e.g.,  $e^+e^- \rightarrow e^+e^-\gamma$ , the condition on the total energy deposition in the calorimeter  $0.3 < E_{\text{tot}}/\sqrt{s} < 0.8$  is applied. The QED processes are additionally suppressed by the requirement that the energy deposition in the calorimeter from charged particles is less than  $0.6\sqrt{s}$ . For events passing the selection criteria described above, the vertex fit is performed using parameters of two charged tracks. The found vertex is used to refine the parameters of charged particles and photons. Then the kinematic fit to the hypothesis  $e^+e^- \rightarrow \pi^+\pi^-\gamma\gamma$  is performed with the four constraints of energy and momentum conservation. As a result of the fit, the momenta of charged parti-

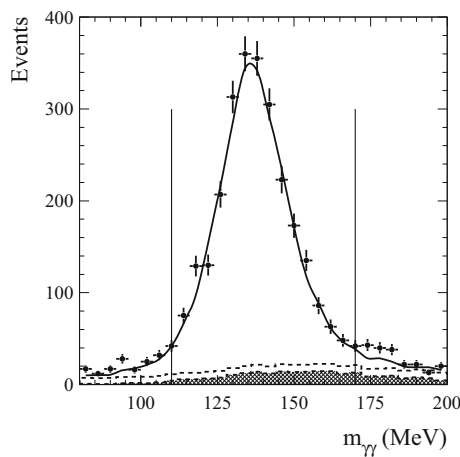


**Fig. 2** The two-photon invariant mass distribution for selected data events from the energy region  $\sqrt{s} = 1.28\text{--}1.52$  GeV (points with error bars). The solid curve is the result of the fit described in the text. The dashed curve shows the total background contribution. The hatched histogram is the distribution for  $e^+e^- \rightarrow \pi^+\pi^-\pi^0\pi^0$  background events. The lines indicate the boundaries of the mass window used in the dynamics study

cles are determined, and the photon energies and angles are refined. The quality of the fit is characterized by the parameter  $\chi^2_{3\pi}$ . The  $\chi^2_{3\pi}$  distribution for data events is compared with the simulated signal+background distribution in Fig. 1. Finally, we select events with  $\chi^2_{3\pi} < 30$  and analyze the two-photon invariant mass ( $m_{\gamma\gamma}$ ) distribution. This distribution for four energy points of the 2012 scan ( $\sqrt{s} = 1.28\text{--}1.52$  GeV) is shown in Fig. 2. It is fitted with a sum of signal and background distributions. The signal distribution is obtained using  $e^+e^- \rightarrow \pi^+\pi^-\pi^0$  simulation.

The main sources of background in the energy region under study are the processes  $e^+e^- \rightarrow \pi^+\pi^-\pi^0\pi^0$  and  $e^+e^- \rightarrow \pi^+\pi^-\gamma$ . The first background process has the  $m_{\gamma\gamma}$  spectrum with a wide maximum to the right of the  $\pi^0$  peak. The shape of the  $m_{\gamma\gamma}$  spectrum for  $e^+e^- \rightarrow \pi^+\pi^-\gamma$  events as well as for other background processes ( $e^+e^- \rightarrow e^+e^-\gamma$ ,  $e^+e^- \rightarrow \mu^+\mu^-\gamma$ ,  $e^+e^- \rightarrow K^+K^-\pi^0$ , ...) is close to linear. In the fit, the background is described by the sum of the simulated distribution for the process  $e^+e^- \rightarrow \pi^+\pi^-\pi^0\pi^0$  and a linear function. The fit parameters are the number of signal events ( $N_{3\pi}$ ), the number of background  $e^+e^- \rightarrow \pi^+\pi^-\pi^0\pi^0$  events ( $N_{4\pi}$ ), and parameters of the linear function. The fitted curve as well as the contributions of the two components of the background are shown in Fig. 2. The fitted  $N_{4\pi}$  value is consistent with the number of  $e^+e^- \rightarrow \pi^+\pi^-\pi^0\pi^0$  events expected from simulation.

The fitted numbers of signal events for the 2012 scan are listed in Table 1 together with the integrated luminosity  $L$ , detection efficiency  $\varepsilon$ , and radiative correction  $1 + \delta$ . The detection efficiency is calculated using the Monte-Carlo simulation performed in the model defined below in Sect. 4. The model includes the intermediate states  $\rho(770)\pi$ ,  $\rho(1450)\pi$ , and  $\omega\pi^0$ . Its parameters are determined in Sect. 4 from a fit to the Dalitz plot distribution and the  $\pi^+\pi^-$  mass spectrum for data events. The model uncertainty of the detection efficiency is estimated by variation of the model parameters within their errors and does not exceed 1%. The detection efficiency is also corrected for the difference between data and simulation in the  $\chi^2_{3\pi}$  distribution and the number of photons in an event. This difference was studied in Ref. [5] and was found to be  $(1.9 \pm 3.1)\%$ .

The radiative correction factor is calculated during the fit to the visible cross section data ( $N_{3\pi}/L$ ) with the

**Table 1** The c.m. energy ( $\sqrt{s}$ ), integrated luminosity ( $L$ ), number of signal events ( $N_{3\pi}$ ), detection efficiency ( $\varepsilon$ ), radiative correction factor ( $1 + \delta$ ), and Born cross section ( $\sigma$ ) for 15 energy points of the 2012 scan. For  $N_{3\pi}$  the statistical error is quoted. For the cross section the first error is statistical, the second is systematic

$\sqrt{s}$ , GeV	$L$ , nb <sup>-1</sup>	$N_{3\pi}$	$\varepsilon$ , %	$1 + \delta$	$\sigma$ , nb
1.28	759.5	$679.2 \pm 35.0$	18.77	0.9123	$5.22 \pm 0.27 \pm 0.23$
1.36	837.4	$638.2 \pm 34.7$	18.77	0.9235	$4.40 \pm 0.24 \pm 0.19$
1.44	1015.6	$713.4 \pm 35.9$	19.07	0.9132	$4.03 \pm 0.20 \pm 0.18$
1.52	670.3	$498.6 \pm 32.6$	19.07	0.8977	$4.34 \pm 0.28 \pm 0.19$
1.68	903.2	$580.5 \pm 34.8$	19.00	0.9409	$3.60 \pm 0.22 \pm 0.16$
1.72	503.6	$211.1 \pm 26.1$	18.18	0.9733	$2.37 \pm 0.29 \pm 0.10$
1.76	894.3	$291.6 \pm 29.5$	18.18	0.9906	$1.81 \pm 0.18 \pm 0.08$
1.80	982.3	$206.9 \pm 26.2$	17.97	0.9974	$1.18 \pm 0.15 \pm 0.05$
1.84	781.9	$146.1 \pm 14.9$	17.70	0.9874	$1.07 \pm 0.11 \pm 0.05$
1.872	919.4	$153.0 \pm 21.7$	16.85	0.9815	$1.01 \pm 0.14 \pm 0.04$
1.90	943.3	$63.4 \pm 26.5$	16.45	0.9628	$0.42 \pm 0.18 \pm 0.02$
1.92	659.5	$60.3 \pm 20.0$	16.53	0.9429	$0.59 \pm 0.19 \pm 0.03$
1.94	923.9	$132.5 \pm 24.4$	15.98	0.9401	$0.95 \pm 0.18 \pm 0.04$
1.96	724.0	$52.0 \pm 17.4$	15.85	0.9369	$0.48 \pm 0.16 \pm 0.02$
1.98	637.1	$56.7 \pm 15.3$	15.42	0.9252	$0.62 \pm 0.17 \pm 0.03$

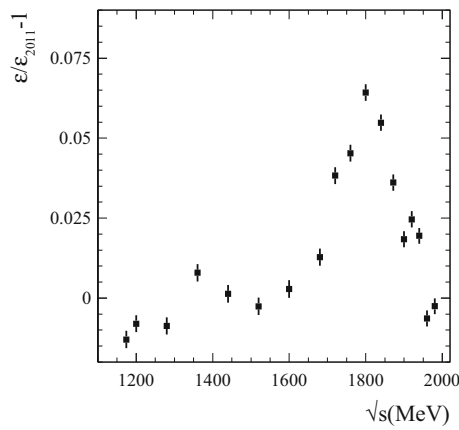


**Fig. 3** The relative difference between the detection efficiency for  $e^+e^- \rightarrow \pi^+\pi^-\pi^0$  events calculated in this work ( $\varepsilon$ ) and the efficiency calculated in Ref. [5] ( $\varepsilon_{2011}$ ) using the model from Ref. [21]

vector–meson–dominance (VMD) model, as described in Ref. [5]. The Born cross section is then calculated as  $\sigma = N_{3\pi} / [\varepsilon L(1 + \delta)]$ .

The detailed analysis of systematic uncertainties on the measured cross section was carried out in Ref. [5]. The total systematic uncertainty is 4.4% and includes the uncertainties in the luminosity measurement(2%), the detection efficiency (3.1%), the numbers of signal events (2%), the radiative correction (1%), and the model error mentioned above (1%).

In the analysis of the 2011 data set [5], the detection efficiency was determined using the simulation based on the model from Ref. [21]. This model includes the  $\rho(770)\pi$ ,  $\rho(1450)\pi$ ,  $\rho(1700)\pi$ , and  $\omega\pi^0$  intermediate states. Its parameters are chosen to reproduce the measured energy dependence of the  $e^+e^- \rightarrow \pi^+\pi^-\pi^0$  cross section and the two-pion invariant mass spectra from Ref. [8]. The relative difference between the detection efficiencies obtained in our model ( $\varepsilon$ ) and in the model [21] ( $\varepsilon_{2011}$ ) as a function of energy is shown in Fig. 3. To understand the source of the about 6%

difference between the models observed near 1.8 GeV, we compare them with the pure  $\rho(770)\pi$  mechanism. The relative difference in the detection efficiency between our model and the  $\rho(770)\pi$  ( $\varepsilon/\varepsilon_{\rho\pi} - 1$ ) is in the range between  $-2\%$  and  $2.5\%$ . Near 1.8 GeV the difference is 1.8%. For the model from Ref. [21] the relative difference  $\varepsilon_{2011}/\varepsilon_{\rho\pi} - 1$  has a minimum in the range 1.7–1.9 GeV. Its minimal value is  $-4.5\%$  at 1.85 GeV. We conclude that the main source of the 6% difference between the models in Fig. 3 is imperfect description of the intermediate states in the  $3\pi$  system in the model of Ref. [21]. Taking this difference as an efficiency correction, we reanalyze the 2011 data. The corrected cross section values are listed in Table 2.

The  $e^+e^- \rightarrow \pi^+\pi^-\pi^0$  cross section obtained in this work in comparison with the BABAR measurement [8], as well as the result of the fit to the SND data with a sum of contributions of isoscalar resonances [5] are shown in Fig. 4.

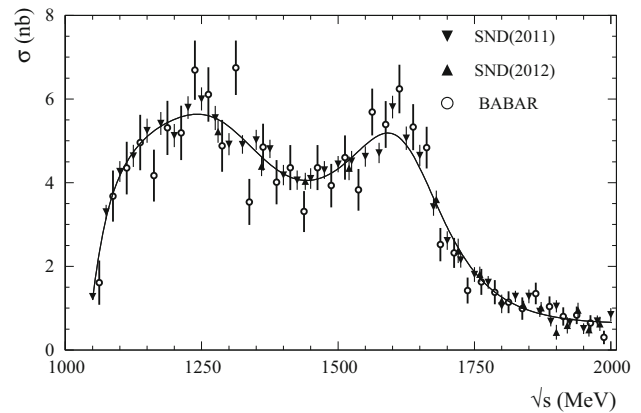


**Fig. 4** The Born cross section for the process  $e^+e^- \rightarrow \pi^+\pi^-\pi^0$  measured in this work for 2011 and 2012 scans, in comparison with the results of the BABAR experiment [8]. The curve represents the result of the fit to the SND data with a sum of contributions from the resonances  $\omega(782)$ ,  $\phi(1020)$ ,  $\omega(1420)$ , and  $\omega(1650)$

**Table 2** The c.m. energy ( $\sqrt{s}$ ) and Born cross section ( $\sigma$ ) for 40 energy points of the 2011 scan. The quoted errors are statistical and systematic, respectively

$\sqrt{s}$ , GeV	$\sigma$ , nb	$\sqrt{s}$ , GeV	$\sigma$ , nb	$\sqrt{s}$ , GeV	$\sigma$ , nb	$\sqrt{s}$ , GeV	$\sigma$ , nb
1.050	$1.27 \pm 0.48 \pm 0.26$	1.300	$4.92 \pm 0.26 \pm 0.22$	1.550	$4.63 \pm 0.24 \pm 0.20$	1.800	$1.05 \pm 0.18 \pm 0.05$
1.075	$3.30 \pm 0.26 \pm 0.40$	1.325	$4.91 \pm 0.22 \pm 0.22$	1.575	$4.71 \pm 0.24 \pm 0.21$	1.825	$1.28 \pm 0.14 \pm 0.06$
1.100	$4.27 \pm 0.32 \pm 0.34$	1.350	$5.02 \pm 0.24 \pm 0.22$	1.600	$5.81 \pm 0.27 \pm 0.26$	1.850	$1.28 \pm 0.17 \pm 0.06$
1.125	$4.64 \pm 0.26 \pm 0.32$	1.375	$4.81 \pm 0.22 \pm 0.21$	1.625	$5.06 \pm 0.28 \pm 0.22$	1.870	$0.92 \pm 0.13 \pm 0.04$
1.150	$5.24 \pm 0.29 \pm 0.31$	1.400	$4.18 \pm 0.24 \pm 0.18$	1.650	$4.65 \pm 0.26 \pm 0.20$	1.890	$0.68 \pm 0.12 \pm 0.03$
1.175	$5.42 \pm 0.27 \pm 0.24$	1.425	$4.06 \pm 0.23 \pm 0.18$	1.675	$3.42 \pm 0.22 \pm 0.15$	1.900	$1.04 \pm 0.15 \pm 0.05$
1.200	$5.13 \pm 0.28 \pm 0.23$	1.450	$4.10 \pm 0.25 \pm 0.18$	1.700	$2.61 \pm 0.23 \pm 0.12$	1.925	$0.66 \pm 0.11 \pm 0.03$
1.225	$5.80 \pm 0.27 \pm 0.26$	1.475	$4.30 \pm 0.21 \pm 0.19$	1.725	$2.15 \pm 0.19 \pm 0.09$	1.950	$0.51 \pm 0.13 \pm 0.02$
1.250	$6.00 \pm 0.28 \pm 0.26$	1.500	$4.44 \pm 0.19 \pm 0.20$	1.750	$1.80 \pm 0.18 \pm 0.08$	1.975	$0.69 \pm 0.14 \pm 0.03$
1.275	$5.55 \pm 0.29 \pm 0.24$	1.525	$4.52 \pm 0.24 \pm 0.20$	1.775	$1.62 \pm 0.16 \pm 0.07$	2.000	$0.84 \pm 0.16 \pm 0.04$

**Table 3** The c.m. energy interval ( $\sqrt{s}$ ), number of selected  $e^+e^- \rightarrow \pi^+\pi^-\pi^0$  events ( $N_{3\pi}$ ), number of background events ( $N_{\text{bkg}}$ ), cross sections for intermediate states  $\rho(770)\pi$  ( $\sigma_{\rho\pi}$ ),  $\rho(1450)\pi$  ( $\sigma_{\rho'\pi}$ ), and  $\omega\pi^0$  ( $\sigma_{\omega\pi}$ ), and relative phases between the amplitudes of the intermediate states  $\rho(1450)\pi$  and  $\rho(770)\pi$  ( $\phi_1$ ), and  $\omega\pi^0$  and  $\rho(770)\pi$  ( $\phi_2$ )

$\sqrt{s}$ , GeV	$N_{3\pi}$	$N_{\text{bkg}}$	$\sigma_{\rho\pi}$ , nb	$\sigma_{\rho'\pi}$ , nb	$\sigma_{\omega\pi}$ , nb	$\phi_1$ , rad	$\phi_2$ , rad
1.15–1.18	957 ± 31	266	4.40 <sup>+0.48</sup> <sub>-0.26</sub>	0.05 <sup>+0.07</sup> <sub>-0.07</sub>	0.21 ± 0.03	–	2.02 <sup>+0.50</sup> <sub>-0.48</sub>
1.20–1.23	1067 ± 33	128	4.68 <sup>+0.32</sup> <sub>-0.24</sub>	0.01 <sup>+0.03</sup> <sub>-0.03</sub>	0.17 ± 0.02	–	1.54 <sup>+0.36</sup> <sub>-0.39</sub>
1.25–1.30	2021 ± 45	241	4.25 <sup>+0.22</sup> <sub>-0.15</sub>	0.06 <sup>+0.09</sup> <sub>-0.09</sub>	0.22 ± 0.02	–	1.28 <sup>+0.22</sup> <sub>-0.23</sub>
1.32–1.38	1642 ± 41	201	4.29 <sup>+0.18</sup> <sub>-0.22</sub>	0.06 <sup>+0.05</sup> <sub>-0.04</sub>	0.26 ± 0.03	–	2.26 <sup>+0.21</sup> <sub>-0.23</sub>
1.42–1.48	1631 ± 40	217	3.43 <sup>+0.25</sup> <sub>-0.28</sub>	0.01 <sup>+0.01</sup> <sub>-0.02</sub>	0.25 ± 0.03	–	1.66 <sup>+0.33</sup> <sub>-0.51</sub>
1.50–1.55	1836 ± 43	217	2.73 <sup>+0.23</sup> <sub>-0.23</sub>	0.25 <sup>+0.10</sup> <sub>-0.10</sub>	0.21 ± 0.03	1.26 <sup>+0.18</sup> <sub>-0.22</sub>	1.82 <sup>+0.24</sup> <sub>-0.28</sub>
1.57–1.60	1679 ± 41	143	2.76 <sup>+0.28</sup> <sub>-0.29</sub>	0.81 <sup>+0.29</sup> <sub>-0.25</sub>	0.14 ± 0.02	1.80 <sup>+0.17</sup> <sub>-0.18</sub>	2.10 <sup>+0.31</sup> <sub>-0.40</sub>
1.65–1.68	1252 ± 35	115	2.12 <sup>+0.22</sup> <sub>-0.23</sub>	0.87 <sup>+0.26</sup> <sub>-0.23</sub>	0.08 ± 0.01	2.30 <sup>+0.17</sup> <sub>-0.16</sub>	2.36 <sup>+0.51</sup> <sub>-1.07</sub>
1.70–1.72	445 ± 21	48	2.02 <sup>+0.26</sup> <sub>-0.26</sub>	0.48 <sup>+0.20</sup> <sub>-0.18</sub>	0.06 ± 0.01	2.67 <sup>+0.18</sup> <sub>-0.25</sub>	1.13 <sup>+1.11</sup> <sub>-0.82</sub>
1.75–1.78	599 ± 24	84	2.00 <sup>+0.24</sup> <sub>-0.25</sub>	0.27 <sup>+0.08</sup> <sub>-0.09</sub>	0.03 ± 0.01	3.27 <sup>+0.35</sup> <sub>-0.40</sub>	3.97 <sup>+0.80</sup> <sub>-0.73</sub>
1.80–1.85	540 ± 23	105	1.20 <sup>+0.20</sup> <sub>-0.24</sub>	0.19 <sup>+0.10</sup> <sub>-0.07</sub>	0.03 ± 0.01	3.21 <sup>+0.45</sup> <sub>-0.47</sub>	3.21 <sup>+1.33</sup> <sub>-1.51</sub>
1.87–1.90	433 ± 21	95	1.14 <sup>+0.11</sup> <sub>-0.15</sub>	0.18 <sup>+0.06</sup> <sub>-0.08</sub>	0.02 ± 0.01	3.84 <sup>+0.17</sup> <sub>-0.36</sub>	2.77 <sup>+0.95</sup> <sub>-1.86</sub>
1.92–1.94	278 ± 17	64	0.30 <sup>+0.12</sup> <sub>-0.11</sub>	0.17 <sup>+0.19</sup> <sub>-0.13</sub>	0.01 ± 0.01	1.63 <sup>+0.44</sup> <sub>-0.40</sub>	1.13 <sup>+1.75</sup> <sub>-1.52</sub>
1.96–2.00	239 ± 15	58	0.32 <sup>+0.10</sup> <sub>-0.10</sub>	0.09 <sup>+0.12</sup> <sub>-0.30</sub>	0.01 ± 0.01	–	0.65 <sup>+3.53</sup> <sub>-1.20</sub>

It is seen that the two SND measurements are in good agreement with each other and with the result of BABAR [8]. The two peaks in the cross section correspond to the  $\omega(1420)$  and  $\omega(1650)$  resonances.

#### 4 Dynamics of the process $e^+e^- \rightarrow \pi^+\pi^-\pi^0$

To study the dynamics of the process  $e^+e^- \rightarrow \pi^+\pi^-\pi^0$ , we analyze the Dalitz plot distribution and the spectrum of the  $\pi^+\pi^-$  invariant mass. Data from 2011 and 2012 scans from the energy range  $\sqrt{s} = 1.15\text{--}2.00$  GeV are used. The range  $\sqrt{s} = 1.05\text{--}1.15$  GeV, in which selected events contain significant fraction of radiative-return  $e^+e^- \rightarrow \phi(1020)\gamma \rightarrow \pi^+\pi^-\pi^0\gamma$  events, is excluded from the analysis. Data with a total integrated luminosity of about  $28 \text{ pb}^{-1}$  are combined into 14 intervals listed in Table 3.

For the Dalitz plot analysis, the event selection criteria are tightened. In addition to the criteria described in Sect. 3 the conditions  $\chi^2_{3\pi} < 20$  and  $110 < m_{\gamma\gamma} < 170$  MeV are applied. The numbers of selected signal and background events in this  $m_{\gamma\gamma}$  range are listed in Table 3 for each energy interval. They are determined from the fit to the  $m_{\gamma\gamma}$  spectrum as described in Sect. 3.

To describe the dynamics of the process  $e^+e^- \rightarrow \pi^+\pi^-\pi^0$ , a model is used, in which the differential cross section is presented as a sum of contributions of the three intermediate states  $\rho(770)\pi$ ,  $\rho(1450)\pi$ , and  $\omega\pi^0$ :

$$\frac{d\sigma}{d\Gamma} = |\alpha A_{\rho\pi} + \beta A_{\rho'\pi} + \gamma A_{\omega\pi}|^2, \tag{1}$$

where  $d\Gamma$  is a phase space element. The amplitudes  $A_{\rho\pi}$ ,  $A_{\rho'\pi}$ , and  $A_{\omega\pi}$  are the functions of  $s$  and pions momenta. For example,  $|A_{\rho\pi}|^2$  is proportional to

$$\sin^2 \theta_n (\mathbf{p}_+ \times \mathbf{p}_-)^2 \left| \sum_k \frac{m_{\rho^k}^2}{q_k^2 - m_{\rho^k}^2 + i q_k \Gamma_{\rho^k}(q_k^2)} \right|^2, \tag{2}$$

where  $\theta_n$  is the angle between the normal to the reaction plane and the beam axis,  $\mathbf{p}_+$  and  $\mathbf{p}_-$  are the charged-pion momenta,

$$\Gamma_{\rho^k}(q_k^2) = \Gamma_{\rho^k} \left( \frac{p_\pi(q_k^2)}{p_\pi(m_{\rho^k}^2)} \right)^3 \frac{m_k^2}{q_k^2}, \tag{3}$$

$k$  takes values  $+, -, 0$ ,  $m_{\rho^k}$  and  $\Gamma_{\rho^k}$  are the mass and width of the  $\rho^k(770)$ ,  $q_k^2$  is the invariant mass of the pion pair,  $p_\pi$  is the pion momentum in the  $\rho$  rest frame.

The  $\rho(1450)\pi$  amplitude is obtained from the  $\rho(770)\pi$  amplitude by replacing the  $\rho(770)$  mass and width with the same parameters for the  $\rho(1450)$ . In the  $\omega\pi^0$  amplitude, the sum over the three charge combinations is replaced by  $m_\omega^2/(q_0^2 - m_\omega^2 + i m_\omega \Gamma_\omega)$ , where  $m_\omega$  and  $\Gamma_\omega$  are the  $\omega$  mass and width. All resonance parameters used in Eq. (1) are taken from the Particle Data Group tables [9].

Other intermediate states, such as  $\rho(1700)\pi$  and the direct transition  $\gamma^* \rightarrow \pi^+\pi^-\pi^0$ , also may contribute to the  $e^+e^- \rightarrow \pi^+\pi^-\pi^0$  reaction. The Dalitz plot distributions for these intermediate states are very similar to that for  $\rho(1450)\pi$ . At our level of statistics we cannot separate these three intermediate states. So, the amplitude  $A_{\rho'\pi}$  effectively describes their total contribution. It should be noted that the



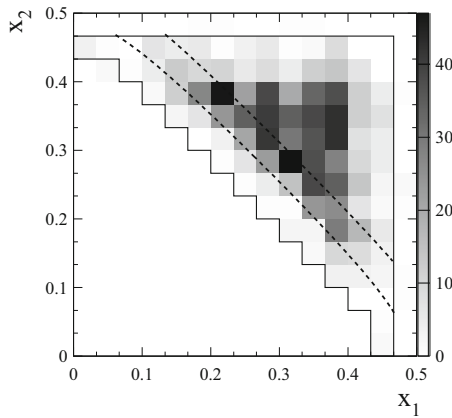


**Fig. 5** The  $x_1$  versus  $x_2$  distribution for selected data events from the interval  $\sqrt{s} = 1.63 - 1.68$  GeV. The solid polygon indicate the Dalitz plot area used in the fit. The area between the dashed curves corresponds to the condition  $0.68 < M_{\pi^+\pi^-} < 0.88$  GeV

$\rho(1700)\pi$  state is suppressed by the phase space compared to the  $\rho(1450)\pi$ . This suppression is by a factor of about 3 in the the  $\omega(1650)$  energy range and grows rapidly with decreasing energy.

The complex coefficients  $\alpha, \beta$  and  $\gamma$  are functions of  $s$  and are determined from a fit to distributions of kinematic variables. The Dalitz plot distribution for data events from the interval  $\sqrt{s} = 1.65-1.68$  GeV is shown in Fig. 5 in the variables  $x_i = p_i/\sqrt{s}$ , where  $p_i$  ( $i = 1, 2$ ) are the charged pion momenta. Since the signs of charged particles are not determined in the SND detector, the indices 1 and 2 are assigned randomly. We perform a binned fit to the Dalitz plot distribution. The bin size is chosen equal  $1/30 \times 1/30$ . The presence of the intermediate mechanism  $\omega\pi^0$  leads to appearance of a narrow structure in the  $\pi^+\pi^-$  invariant mass ( $M_{\pi^+\pi^-}$ ) spectrum near the  $\omega$  mass, for description of which the chosen binning is too coarse. Therefore, events with  $0.68 < M_{\pi^+\pi^-} < 0.88$  GeV are excluded from the Dalitz plot distribution. A one-dimensional  $M_{\pi^+\pi^-}$  distribution is constructed for them with a 10 MeV bin. The Dalitz plot distribution and the  $M_{\pi^+\pi^-}$  distribution are fitted simultaneously.

To take into account detector resolution and dependence of the detection efficiency on position in the Dalitz plot, the fitting function for the data Dalitz plot distribution is constructed as follows:

$$\begin{aligned}
 D(s, x_1, x_2) = & |\alpha|^2 H_{\rho\pi} + |\beta|^2 H_{\rho'\pi} + |\gamma|^2 H_{\omega\pi} \\
 & + 2|\alpha||\beta| \cos(\phi_1) R_{\rho\pi-\rho'\pi} \\
 & + 2|\alpha||\beta| \sin(\phi_1) I_{\rho\pi-\rho'\pi} \\
 & + 2|\alpha||\gamma| \cos(\phi_2) R_{\rho\pi-\omega\pi} \\
 & + 2|\alpha||\gamma| \sin(\phi_2) I_{\rho\pi-\omega\pi} \\
 & + 2|\beta||\gamma| \cos(\phi_2 - \phi_1) R_{\rho'\pi-\omega\pi} \\
 & + 2|\beta||\gamma| \sin(\phi_2 - \phi_1) I_{\rho'\pi-\omega\pi}, \tag{4}
 \end{aligned}$$

where  $H_{\rho\pi}, H_{\rho'\pi}$ , and  $H_{\omega\pi}$  are the distributions corresponding to the moduli squared of the amplitudes  $A_{\rho\pi}, A_{\rho'\pi}$ , and  $A_{\omega\pi}$ , respectively. They are calculated using MC simulation. For example, to obtain  $H_{\rho\pi}$ , a simulation is performed in the model described by Eq. (1) with  $\alpha = 1$  and  $\beta = \gamma = 0$ . The simulation takes into account radiation corrections [22], which are calculated using the Born cross section shown in Fig. 4. Simulated events pass the selection criteria described above. For selected events, a two-dimensional  $x_1$  versus  $x_2$  distribution is constructed. Also the detection efficiency  $\varepsilon_{\rho\pi}$  and the cross section  $\sigma_{\rho\pi, \text{vis}} = (1 + \delta) \int |A_{\rho\pi}|^2 d\Gamma$ , where  $\delta$  is the radiative correction, are calculated. The efficiency is corrected for the data-simulation difference as described in Sect. 3. The resulting distribution is normalized to the expected number of events

$$\varepsilon_{\rho\pi}(s_i) \sigma_{\rho\pi, \text{vis}}(s_i) L_i, \tag{5}$$

where  $L_i$  is the integrated luminosity for the  $i$ th energy interval.

The distributions  $R_{i-j}$  and  $I_{i-j}$  correspond to the real and imaginary parts of the interference terms  $A_i A_j^*$  ( $i \neq j$ ), where  $i$  and  $j$  are  $\rho\pi, \rho'\pi$ , and  $\omega\pi$ . To obtain, for example, the distributions  $R_{\rho\pi-\rho'\pi}$  and  $I_{\rho\pi-\rho'\pi}$ , two simulations are performed using Eq. (1) with  $\alpha = 1, \beta = 1$  and  $\gamma = 0$ , and with  $\alpha = 1, \beta = i$  and  $\gamma = 0$ , and the distributions  $H_{\rho\pi+\rho'\pi}$  and  $H_{\rho\pi+i\rho'\pi}$  are constructed, as it is described above for  $H_{\rho\pi}$ . Then we determine

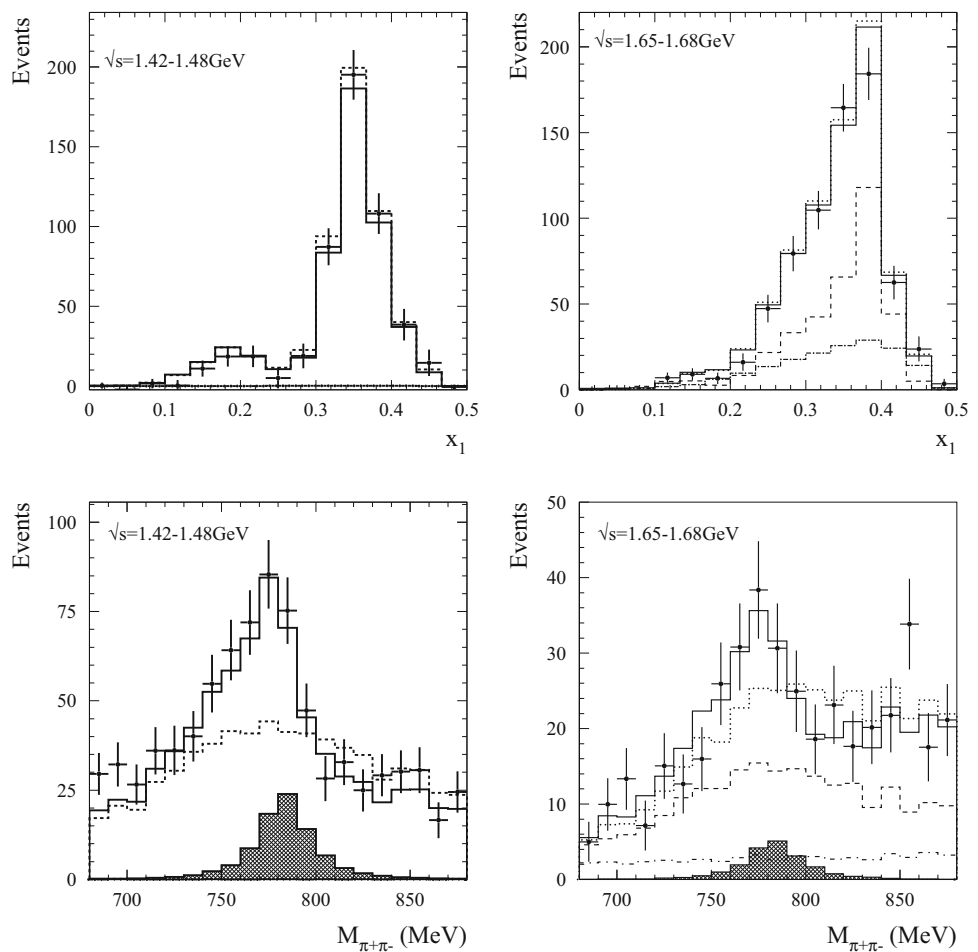
$$\begin{aligned}
 2R_{\rho\pi-\rho'\pi} &= H_{\rho\pi+\rho'\pi} - H_{\rho\pi} - H_{\rho'\pi}, \\
 2I_{\rho\pi-\rho'\pi} &= H_{\rho\pi+i\rho'\pi} - H_{\rho\pi} - H_{\rho'\pi}. \tag{6}
 \end{aligned}$$

The distributions with the indices  $\rho\pi - \omega\pi$  and  $\rho'\pi - \omega\pi$  are built in the same way. The same technique is used for the  $M_{\pi^+\pi^-}$  distribution.

The distributions for background events are obtained using simulation of the processes  $e^+e^- \rightarrow \pi^+\pi^-\pi^0\pi^0$  [23] and  $e^+e^- \rightarrow \pi^+\pi^-\gamma$ . These two processes produce about 80% of background events. The simulated distributions are normalized to the number of background events listed in Table 3. It is tested that this background model describes well the distribution of two-pion masses for the control regions  $80 < m_{\gamma\gamma} < 110$  MeV and  $170 < m_{\gamma\gamma} < 200$  MeV.

Due to the interference between the intermediate states  $\rho(770)\pi$  and  $\omega\pi^0$ , the  $M_{\pi^+\pi^-}$  spectrum has a narrow peak-dip structure near the  $\omega$  mass (see, for example [15]). The shape of this structure depends on the phase  $\phi_2$ . The detector resolution smears the interference pattern. Therefore, only a peak is observed in the experimental spectrum. This leads to a very strong correlation between the parameters  $|\gamma|$  and  $\phi_2$  extracted from the fit to the  $\pi^+\pi^-$  mass spectrum. The parameter  $|\gamma|$  can, however, be determined from the Born cross section of the process  $e^+e^- \rightarrow \omega\pi^0 \rightarrow \pi^0\pi^0\gamma$

**Fig. 6** The  $x_1$  distribution and  $M_{\pi^+\pi^-}$  spectrum for two energy intervals:  $\sqrt{s} = 1.42\text{--}1.48$  MeV and  $\sqrt{s} = 1.65\text{--}1.68$  MeV. The points with error bars represent data. The solid histogram is the result of the fit described in the text. The dashed, dash-dotted, and hatched histograms show the distributions corresponding to the squared amplitudes for the intermediate states  $\rho(770)\pi$ ,  $\rho(1450)\pi$  and  $\omega\pi^0$ , respectively. The dotted histograms in the right plots show the total contributions of the  $\rho(770)\pi$  and  $\rho(1450)\pi$  intermediate states including the interference term



( $\sigma_{\pi^0\pi^0\gamma}$ ) measured by SND [24]:

$$\begin{aligned} \sigma_{\omega\pi}(s_i) &= |\gamma(s_i)|^2 \int |A_{\omega\pi}(s_i)|^2 d\Gamma \\ &= \sigma_{\pi^0\pi^0\gamma}(s_i) \frac{B(\omega \rightarrow \pi^+\pi^-)}{B(\omega \rightarrow \pi^0\gamma)}, \end{aligned} \quad (7)$$

where  $B(\omega \rightarrow \pi^+\pi^-)$  and  $B(\omega \rightarrow \pi^0\gamma)$  are the branching fractions of the corresponding  $\omega$  decays [9]. The values of the cross section  $\sigma_{\omega\pi}$  obtained using Eq. (7) are given in Table 3. During the fit the parameter  $|\gamma|$  is allowed to vary within its errors near the calculated value.

Instead of the parameters  $|\alpha|$  and  $|\beta|$ , we use the Born cross sections for the  $\rho(770)\pi$  and  $\rho(1450)\pi$  mechanisms:

$$\begin{aligned} \sigma_{\rho\pi}(s_i) &= |\alpha(s_i)|^2 \int |A_{\rho\pi}(s_i)|^2 d\Gamma, \\ \sigma_{\rho'\pi}(s_i) &= |\beta(s_i)|^2 \int |A_{\rho'\pi}(s_i)|^2 d\Gamma. \end{aligned} \quad (8)$$

These cross sections, as well as the relative phases  $\phi_1$  and  $\phi_2$ , are determined from the fit to the Dalitz plot distribution and the  $M_{\pi^+\pi^-}$  spectrum.

The data  $x_1$  and  $M_{\pi^+\pi^-}$  distributions for the energy intervals  $\sqrt{s} = 1.42\text{--}1.48$  MeV and  $\sqrt{s} = 1.65\text{--}1.68$  MeV are

shown in Fig. 6. The distributions obtained as a result of the fit are also shown together with the spectra corresponding to the squares of the  $\rho(770)\pi$ ,  $\rho(1450)\pi$ , and  $\omega\pi^0$  amplitudes ( $|\alpha|^2 H_{\rho\pi}$ ,  $|\beta|^2 H_{\rho'\pi}$ , and  $|\gamma|^2 H_{\omega\pi}$ ). The relative fraction of the intermediate mechanism, for example  $\rho\pi$ , is defined as follows:

$$f_{\rho\pi} = \frac{\int d\Gamma |\alpha A_{\rho\pi}|^2}{\int d\Gamma |\alpha A_{\rho\pi} + \beta A_{\rho'\pi} + \gamma A_{\omega\pi}|^2}. \quad (9)$$

At  $\sqrt{s} \approx 1.45$  GeV  $f_{\rho\pi} = (84 \pm 7)\%$ ,  $f_{\rho'\pi} = (0.2 \pm 0.4)\%$ , and  $f_{\omega\pi} = (6 \pm 1)\%$ . The interference between the isovector ( $\omega\pi^0$ ) and isoscalar ( $\rho\pi + \rho'\pi$ ) amplitudes give a 10% contribution to the total  $e^+e^- \rightarrow \pi^+\pi^-\pi^0$  cross section. Thus, the total contribution associated with the intermediate state  $\omega\pi^0$  is 16%. This contribution should be subtracted from the cross section if it is used to determine the parameters of the  $\omega(1420)$  and  $\omega(1650)$  resonances.

Figure 6 shows that the  $\rho(1450)\pi$  contribution becomes essential at  $\sqrt{s} \approx 1.67$  GeV:  $f_{\rho\pi} = (55 \pm 6)\%$ ,  $f_{\rho'\pi} = (24 \pm 7)\%$ . The contribution of the interference between these states is about 22%. The fraction  $f_{\omega\pi} = (2.1 \pm 0.4)\%$ , and the interference with isoscalar states is approximately  $-2\%$ .

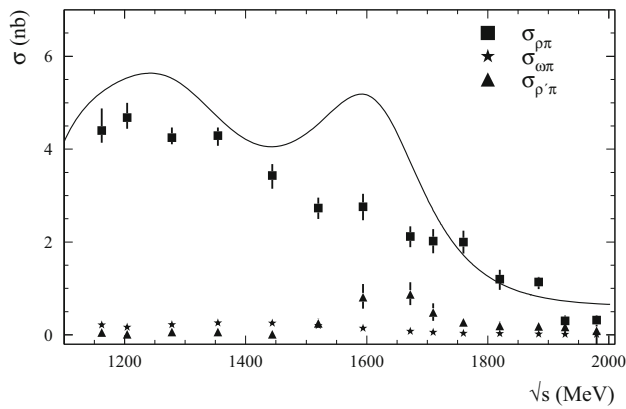


**Fig. 7** The measured energy dependences of the cross sections  $\sigma_{\rho\pi}$ ,  $\sigma_{\rho'\pi}$ , and  $\sigma_{\omega\pi}$ . The curve is the result of the fit to the SND data on the total  $e^+e^- \rightarrow \pi^+\pi^-\pi^0$  cross section (see Fig. 4)

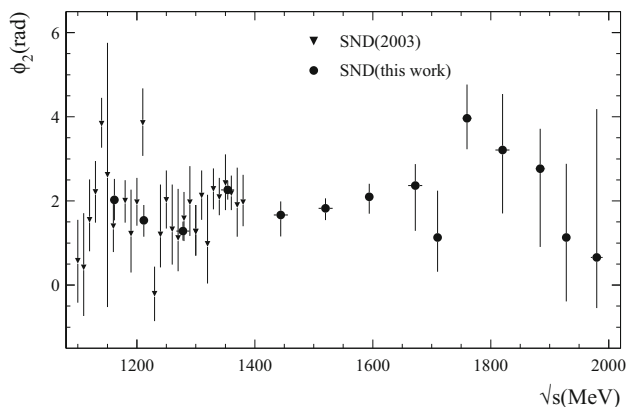


**Fig. 8** The relative phase between the  $\omega\pi^0$  and  $\rho(770)\pi$  amplitudes measured in this work in comparison with the results of Ref. [3]

The fit parameters for all 14 energy intervals are listed in Table 3. In the intervals, in which  $\sigma_{\rho'\pi}$  is consistent with zero, the phase  $\phi_1$  cannot be determined from the fit. Figure 7 shows the energy dependences of the cross sections  $\sigma_{\rho\pi}$ ,  $\sigma_{\rho'\pi}$ , and  $\sigma_{\omega\pi}$  in comparison with the total  $e^+e^- \rightarrow \pi^+\pi^-\pi^0$  cross section (curve from Fig. 4). It is seen that the cross section  $\sigma_{\rho'\pi}$  differs from zero in the region of the second maximum in the  $e^+e^- \rightarrow \pi^+\pi^-\pi^0$  cross section, corresponding to the  $\omega(1650)$  resonance. In the cross section  $\sigma_{\rho\pi}$  the resonance structure near 1650 MeV is not seen. We conclude that the intermediate state  $\rho(1450)\pi$  gives a significant contribution to the decay of  $\omega(1650) \rightarrow \pi^+\pi^-\pi^0$ , while the  $\rho(770)\pi$  dominates in the  $\omega(1420) \rightarrow \pi^+\pi^-\pi^0$  decay.

Figure 8 shows the energy dependence of the relative phase  $\phi_2$  between the  $\omega\pi^0$  and  $\rho(770)\pi$  amplitudes. In the region  $\sqrt{s} = 1.15\text{--}1.55$  GeV, it is close to  $\pi/2$ . It should be noted that a phase shift of approximately  $\pi/2$  is generated by the  $\rho - \omega$  mixing [3, 15], which is the dominant mechanism of the  $\omega \rightarrow \pi^+\pi^-$  decay. Below 1.4 GeV our result

agrees with the measurement of Ref. [3]. In this work,  $A_{\omega\pi}$  is parametrized taking into account the  $\rho - \omega$  mixing. For comparison with our measurement,  $\pi/2$  is added to the results from Ref. [3].

## 5 Summary

In the experiment with the SND detector at the VEPP-2000  $e^+e^-$  collider, the dynamics of the process  $e^+e^- \rightarrow \pi^+\pi^-\pi^0$  has been studied in the c.m. energy range from 1.15 to 2.00 GeV. The  $\pi^+\pi^-$  invariant mass spectra and the two-dimensional distribution of the momenta of charged pions have been fitted with the model including the  $\rho(770)\pi$ ,  $\rho(1450)\pi$ , and  $\omega\pi^0$  intermediate states. The modulus squared of the  $\omega\pi^0$  amplitude has been fixed from our measurement of the  $e^+e^- \rightarrow \omega\pi^0 \rightarrow \pi^0\pi^0\gamma$  cross section [24]. As a result of the fit, the cross sections for the intermediate states  $\rho(770)\pi$  and  $\rho(1450)\pi$ , and the relative phases between the  $\rho(770)\pi$  amplitude and the  $\rho(1450)\pi$  and  $\omega\pi^0$  amplitudes have been obtained for 14 energy intervals. The cross section for the intermediate state  $\rho(1450)\pi$  differs significantly from zero in the range 1.55–1.75 GeV, where the resonance  $\omega(1650)$  is located. In the  $\rho(770)\pi$  cross section the resonance structure near 1650 MeV is not observed. We conclude that the intermediate state  $\rho(1450)\pi$  gives a significant contribution to the decay  $\omega(1650) \rightarrow \pi^+\pi^-\pi^0$ , and that the  $\omega(1420) \rightarrow \pi^+\pi^-\pi^0$  decay is dominated by the  $\rho(770)\pi$  intermediate state.

As a result of the refinement of the model describing the  $e^+e^- \rightarrow \pi^+\pi^-\pi^0$  internal structure, the correction has been determined for the detection efficiency, which was previously calculated in the model of Ref. [21]. This correction is maximal at  $\sqrt{s} = 1.8$  GeV, where it is about 7%. With this correction the measurement of the  $e^+e^- \rightarrow \pi^+\pi^-\pi^0$  cross section based on the 2011 data set [5] has been updated. The cross section has been also measured using the 2012 data set. Both measurements are consistent with each other and with the result of the BABAR experiment [8]. The data on the cross section for the process  $e^+e^- \rightarrow \pi^+\pi^-\pi^0$ , obtained in this work, refine and replace the data of Ref. [5].

**Acknowledgements** This work is supported by the RFBR Grant no. 20-02-00060-a.

**Data Availability Statement** This manuscript has no associated data or the data will not be deposited. [Authors' comment: The data generated during this analysis (number of events, efficiency, cross sections, etc) are presented in the tables and plots of this article.]

**Open Access** This article is licensed under a Creative Commons Attribution 4.0 International License, which permits use, sharing, adaptation, distribution and reproduction in any medium or format, as long as you give appropriate credit to the original author(s) and the source, provide a link to the Creative Commons licence, and indicate if changes



were made. The images or other third party material in this article are included in the article's Creative Commons licence, unless indicated otherwise in a credit line to the material. If material is not included in the article's Creative Commons licence and your intended use is not permitted by statutory regulation or exceeds the permitted use, you will need to obtain permission directly from the copyright holder. To view a copy of this licence, visit <http://creativecommons.org/licenses/by/4.0/>.

Funded by SCOAP<sup>3</sup>.

## References

1. J.E. Augustin et al., Phys. Lett. B **28**, 513 (1969)
2. M.N. Achasov et al., SND Collaboration. Phys. Rev. D **63**, 072002 (2001)
3. M.N. Achasov et al., SND Collaboration. Phys. Rev. D **66**, 032001 (2002)
4. M.N. Achasov et al., SND Collaboration. Phys. Rev. D **68**, 052006 (2003)
5. V.M. Aul'chenko et al., SND Collaboration. J. Exp. Theor. Phys. **121**, 27 (2015)
6. R.R. Akhmetshin et al., CMD-2 Collaboration. Phys. Lett. B **578**, 285 (2004)
7. R.R. Akhmetshin et al., CMD-2 Collaboration. Phys. Lett. B **642**, 203 (2006)
8. B. Aubert et al., BABAR Collaboration. Phys. Rev. D **70**, 072004 (2004)
9. M. Tanabashi et al., Particle Data Group. Phys. Rev. D **98**, 030001 (2018)
10. G.S. Adams et al., CLEO Collaboration. Phys. Rev. D **73**, 012002 (2006)
11. M. Ablikim et al., BESIII Collaboration. Phys. Rev. D **98**, 112007 (2018)
12. A. Aloisio et al. (KLOE Collaboration), Phys. Lett. B **561**, 55 (2003) (**Erratum: [Phys. Lett. B 609, 449 (2005)]**)
13. J.P. Lees et al., BABAR Collaboration. Phys. Rev. D **95**, 072007 (2017)
14. M. Ablikim et al., BESIII Collaboration. Phys. Lett. B **710**, 594 (2012)
15. N.N. Achasov, A.A. Kozhevnikov, G.N. Shestakov, Phys. Lett. B **50**, 448 (1974)
16. A. Romanov et al., in *Proceedings of PAC 2013, Pasadena, CA USA*, p. 14
17. M.N. Achasov et al., Nucl. Instrum. Methods A **598**, 31 (2009)
18. V.M. Aulchenko et al., Nucl. Instrum. Methods A **598**, 102 (2009)
19. A.Y. Barnyakov et al., Nucl. Instrum. Methods A **598**, 163 (2009)
20. V.M. Aulchenko et al., Nucl. Instrum. Methods A **598**, 340 (2009)
21. H. Czyz, A. Grzelinska, J.H. Kuhn, G. Rodrigo, Eur. Phys. J. C **47**, 617 (2006)
22. E.A. Kuraev, V.S. Fadin, Sov. J. Nucl. Phys. **41**, 466 (1985)
23. H. Czyz, J.H. Kuhn, A. Wapientnik, Phys. Rev. D **77**, 114005 (2008)
24. M.N. Achasov et al., SND Collaboration. Phys. Rev. D **94**, 112001 (2016)